AIMS Materials Science, 3(4): 1632-1648.
DOI: 10.3934/matersci.2016.4.1632
Received: 25 September 2016
Accepted: 15 November 2016
Published: 28 November 2016

http://www.aimspress.com/journal/Materials

Research article

Investigating surface morphology and cracking during lithiation of Al anodes

Omid Gooranorimi and Ali Ghahremaninezhad *

Department of Civil, Architectural and Environmental Engineering, University of Miami, Coral Gables, FL 33146, United States

* **Correspondence**: Email: a.ghahremani@miami.edu; Tel: +1-305-2843465.

Abstract: This paper examines morphology and crack formation in Al anodes during lithiation. The morphological evolution during the lithiation of Al foils was studied using optical and scanning electron microscopy (SEM). X-ray diffraction (XRD) was utilized to evaluate the structural changes, and the uniaxial tensile test was employed to study the mechanical properties of lithiated Al. It was observed that the lithiation of Al consisted of nucleation and growth of LiAl nodules on the surface and their columnar growth in the thickness direction. Cracks were observed to initiate near the nodule peak and at the boundary between nodules. The effect of charge rate on the crystallite size and surface nodule size of LiAl is discussed. It was found that the stiffness and fracture strength of LiAl were lower than those of pristine Al.

Keywords: lithiation; Al anodes; cracks; nodules; SEM microscopy

1. Introduction

Lithium-ion batteries are projected to be the leading energy source for electrification of electric drive vehicles in addition to providing a reliable means for energy storage. While lithium-ion batteries have found widespread applications in portable electronics and power tools, their implementation in high energy and large size applications, such as electric drive vehicles, requires an improved specific capacity and cycle life in order to meet stringent government and industry regulations. In the search for high capacity lithium-ion batteries, metal anodes such as silicon, tin,

germanium and aluminum, among others, have emerged that possess a theoretical specific charge capacity significantly greater than their conventional graphite counterpart [1–5]. In spite of their high capacity, metal anode based lithium-ion batteries have shown poor structural integrity and cycle life, which has been the bottleneck to the large scale implementation of these kinds of batteries. This issue arises from the large dimensional changes that accompany the phase transformations during lithiation/delithiation (alloying/dealloying with/from lithium) in metal anodes [1,6–12]. The large dimensional changes induce deformation gradients in constrained metal anodes, leading to stress and eventually crack formation in metal anodes [13,14]. Crack formation reduces the electric conductivity of the metal anodes and also inhibits the formation of a stable solid electrolyte interface (SEI) due to the continuous creation of new surfaces during cracking [15].

Aluminum (Al) as an anode material in lithium-ion batteries has been extensively studied by several researchers in the past [16–27]. Upon alloying Al with Li, the intermetallic phase Li_xAl forms with an increase in molar volume relative to Al. Large dimensional changes due to phase transformation during the lithiation of Al anodes have been identified to develop mechanical stress, ultimately resulting in cracking and poor electrochemical behavior [21,28–31]. This points to the importance of mechanical integrity in the performance of Al anodes and the underlying mechanisms determining the mechanical behavior and fracture processes of Al anodes during lithiation and delithiation in lithium-ion batteries. In spite of prior investigations, most of the studies on Al anodes have focused on the thermodynamics and kinetics of electrochemical alloying [17,32,33] and capacity and cycle life measurements [22,23,24,26,27,28] of Al anodes. Although, it is generally accepted that failure in Al anodes is attributed to large volumetric changes, the details of the mechanisms responsible for crack formation and material disintegration in Al anodes have not received much attention and are currently poorly understood. To highlight the importance of studying the mechanisms of failure, it is noted that cracks are commonly believed to form in metal anodes during delithiation, when the metal anodes are in tension. In this study, it is shown that cracks can occur during lithiation and an explanation for such behavior is presented.

This study aims to investigate the morphological evolution and crack formation associated with the lithiation of Al foils. In this paper, surface morphology and atomic structure of lithiated Al were studied using microscopy and X-ray diffraction (XRD), respectively. The change in the mechanical properties of lithiated Al as a result of lithiation was evaluated using tensile testing at the microscale. The effect of current density on surface morphology and crystallite size of lithiated Al is discussed.

2. Materials and Methods

2.1. Lithiation Test

Lithiation of Al was performed using foils (99% purity) of thickness 50 μm. Strips with dimensions of 1.7 × 16 mm were cut from the foils, cleaned with acetone, and mounted on a microscope glass slide with one end attached to a glass tab with a double-sided tape and the other end free. The schematics of the Al foils and the mounting fixture, and the electrochemical cell are shown in Figure 1a and 1b, respectively. Such a setup allows for easy handling of the specimens for SEM and XRD studies as well as for mounting them on a microtensile stage for mechanical testing,

as described later in this paper. A copper adhesive tape was used at the end of the Al foils to provide electrical connection to a Gamry 600 Reference Potentiostat. A polyethylene (PE) adhesive tape was used to mask a 4 mm length at the ends of the Al foils. The other end of the Al foils was left free to allow lithiation induced elongation without any stress development due to a constraint. Specimens were transferred to an argon-filled glovebox for electrochemical lithiation. A lithium foil of thickness 0.75 mm, to serve as both the counter and reference electrodes, was attached to a nickel wire and connected to the electrochemical analyzer. Both electrodes were submerged in an electrolyte consisting of a solution of 1 M lithium salt $LiFP_6$ in a mixture of 1:1 by volume of ethylene carbonate and diethyl carbonate (EC:DEC). This electrolyte is commonly used in the study of Li-ion batteries [33,34]. Both sides of Al foils were exposed to the electrolyte and, therefore, subjected to lithiation. Specimens were lithiated to various levels of charge corresponding to 378 mAh/g, 576 mAh/g, and 922 mAh/g. Lithiation occurred at a current density of 0.18 mA/cm^2. The theoretical charge capacity of the Li_xAl anode in a lithium-ion battery at room temperature is about 990 mAh/g corresponding to $x = 1$ [28,30].

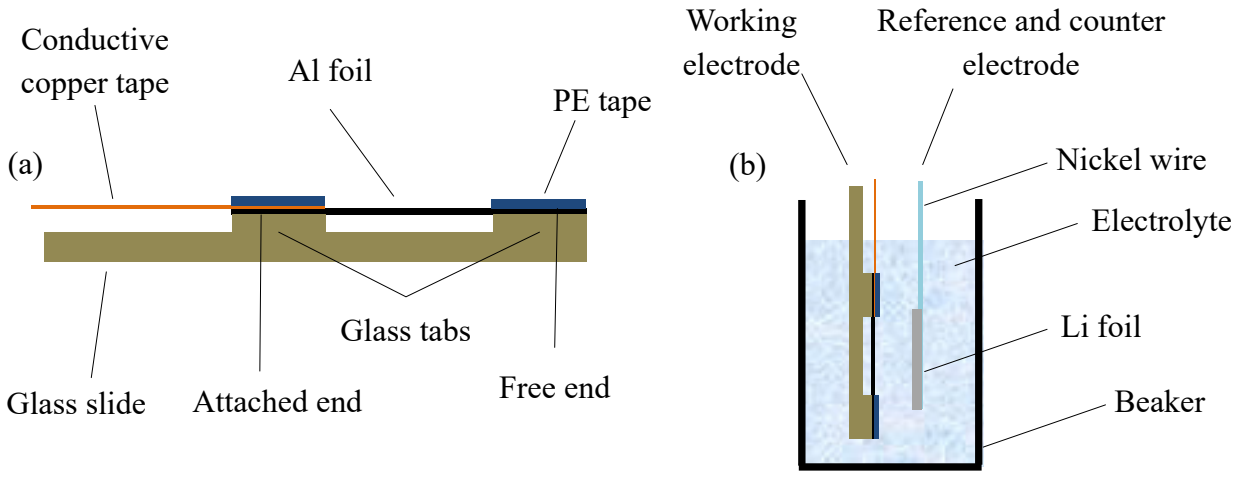

Figure 1. (a) Schematic of the Al foils and the mounting fixture used in the lithiation study of Al. (b) Schematic of the electrochemical cell.

After lithiation, Al foils were taken out of the electrolyte, rinsed with diethyl carbonate, and dried in the glovebox for several hours. In order to examine the morphology of specimens subjected to lithiation, scanning electron microscopy was utilized. Specimens were sealed in polypropylene tubes during the transfer to an FEI XL-30 Field Emission ESEM/SEM to protect them from exposure to air and moisture.

In order to evaluate the change in the structure of lithiated Al foils, other specimens were lithiated and used for XRD. The XRD analysis was carried out in a Philips X'Pert X-ray diffractometer with Cu Kα radiation at a scan rate of 8 sec/step and 0.004 degree/step. An estimate of the crystallite size of the lithiated Al foils was obtained from the diffraction widths of the spectra using the Scherrer equation [35] as follows:

$$d = \frac{0.9\lambda}{\beta \cos\theta} \tag{1}$$

where λ is the X-ray beam wavelength, θ is the peak angle, and β is the full width at half-maximum of the peak diffraction.

3. Results and Discussion

3.1. Microscopic Examination

All Al foils showed a lithiation plateau at about 0.2–0.3 V, which was in agreement with previous studies [24,36]. Figures 2a, 2c, and 2e show the SEM images of Al foils lithiated to 378 mAh/g, 576 mAh/g, and 922 mAh/g, respectively. As mentioned previously, the theoretical charge capacity of Li_xAl, corresponding to x = 1, at room temperature is 990 mAh/g; thus, the specimen with the highest lithiation level is considered near full lithiation. However, some charges are consumed due to irreversible processes at the beginning of the lithiation. It is seen that the surface of the Al foils demonstrated nodular features; the density of nodules is observed to increase with increasing levels of lithiation. As discussed later, XRD analysis indicated that these nodules were the lithiation product LiAl phase. Figure 2b depicts a nodule during the early stage of lithiation; plastic slip lines are easily seen on the Al foil surface adjacent to the nodule, indicating large local plastic deformations as a result of increased volumetric change accompanying nodule formation. Figures 2d and 2f show higher magnification SEM images of cracks on the surface of Al foils corresponding to Figures 2c and 2e, respectively. The following observations were made from the SEM microscopy.

- It is seen that at the lithiation level of 378 mAh/g, several nodules of LiAl have been nucleated and grown. With continued lithiation, more nodules formed and partially covered the surface of the specimen, as seen in Figure 2c, corresponding to a lithiation level of 576 mAh/g. Cracks are seen to form on the surface as seen in Figures 2c and 2d. The cracks seem to occur near the nodule peaks as well as at the nodule boundaries. No cracks were detected on the surface of the specimen lithiated to 378 mAh/g and cracks were observed on the surface of the specimen lithiated to 576 mAh/g in regions where nodules coalesced and covered a portion of the surface.
- Finally, at the lithiation level of 922 mAh/g, the surface of the specimen was entirely covered by the nodules and cracks are observed to have formed on the surface of the Al specimen (see Figure 2e). A higher magnification image of such cracks is shown in Figure 2f. The average nodule size on the specimen lithiated to 922 mAh/g was measured to be about 30 μm using the image analysis software ImageJ.
- In order to understand the lithiation progress in the thickness direction, the SEM image showing the cross section of Al foil lithiated to about 800 mAh/g is shown in Figure 3a. Lithiated and unlithiated portions of the cross section are marked in the figure. It appears that the surface nodules have exhibited a columnar growth in the thickness direction during lithiation. The plan view of the interface between the lithiated and unlithiated portions of the Al foil is shown in Figure 3b. It is seen that the surface consists of dimples indicating the wavy morphology of the interface between the lithiated and unlithiated portions in the thickness direction of the specimens.
- A correlation can be made between the morphology of the interface (Figure 3b) and that of the nodules on the surface from Figure 3a. The dimples on the interface are of similar size to the

nodules on the surface of Al foil, which were estimated to be about 30 μm. An estimate of the nodule height in the range of 5–10 μm can be made from Figure 3a.

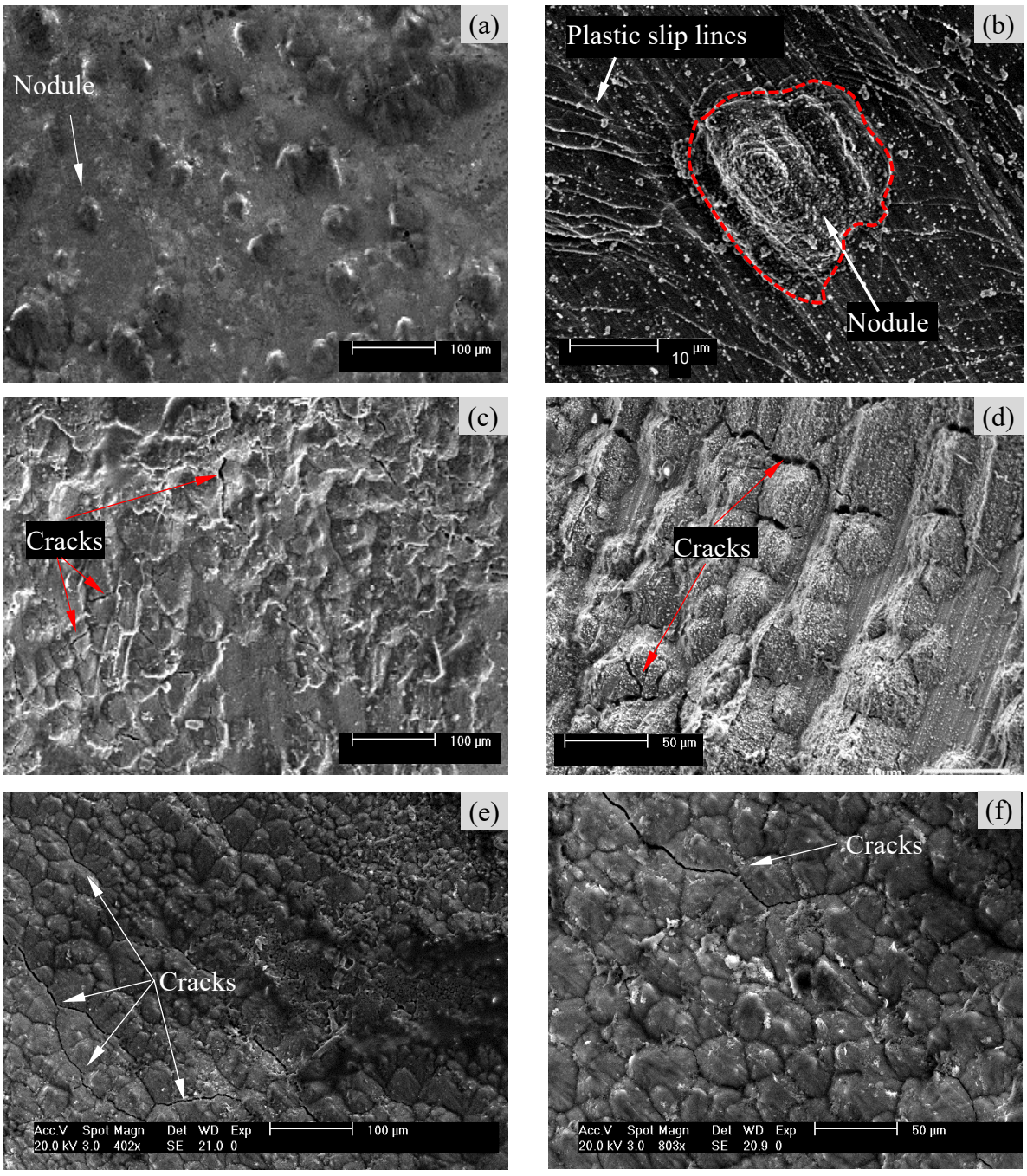

Figure 2. SEM images of Al foils lithiated to (a) 378 mAh/g, (c) 576 mAh/g, and (e) 922 mAh/g, respectively. (b) Higher magnification SEM image showing a LiAl nodule formation in the early stage of lithiation; plastic slip lines can be observed on the surface of Al indicating a large local plastic deformation as a result of volumetric change of LiAl. The nodule is delimited by a red dashed line. (d) and (f) Higher magnification SEM images showing cracks on the surface of Al foils corresponding to (c) and (e), respectively.

- An optical micrograph of the cross section of a different Al foil, partially lithiated, is shown in Figure 3c. After lithiation, this specimen was cut, set in epoxy, and subsequently polished with SiC sand papers of grit sizes 80, 320, 600, and 1200, using acetone as a lubricant. The final polishing was achieved using 3 μm and 1 μm polycrystalline diamond abrasives. The lithiated and unlithiated portions are marked in the figure. Multiple cracks are clearly evident in this figure and some of the cracks penetrated through the entire lithiated portion and stopped at the interface.

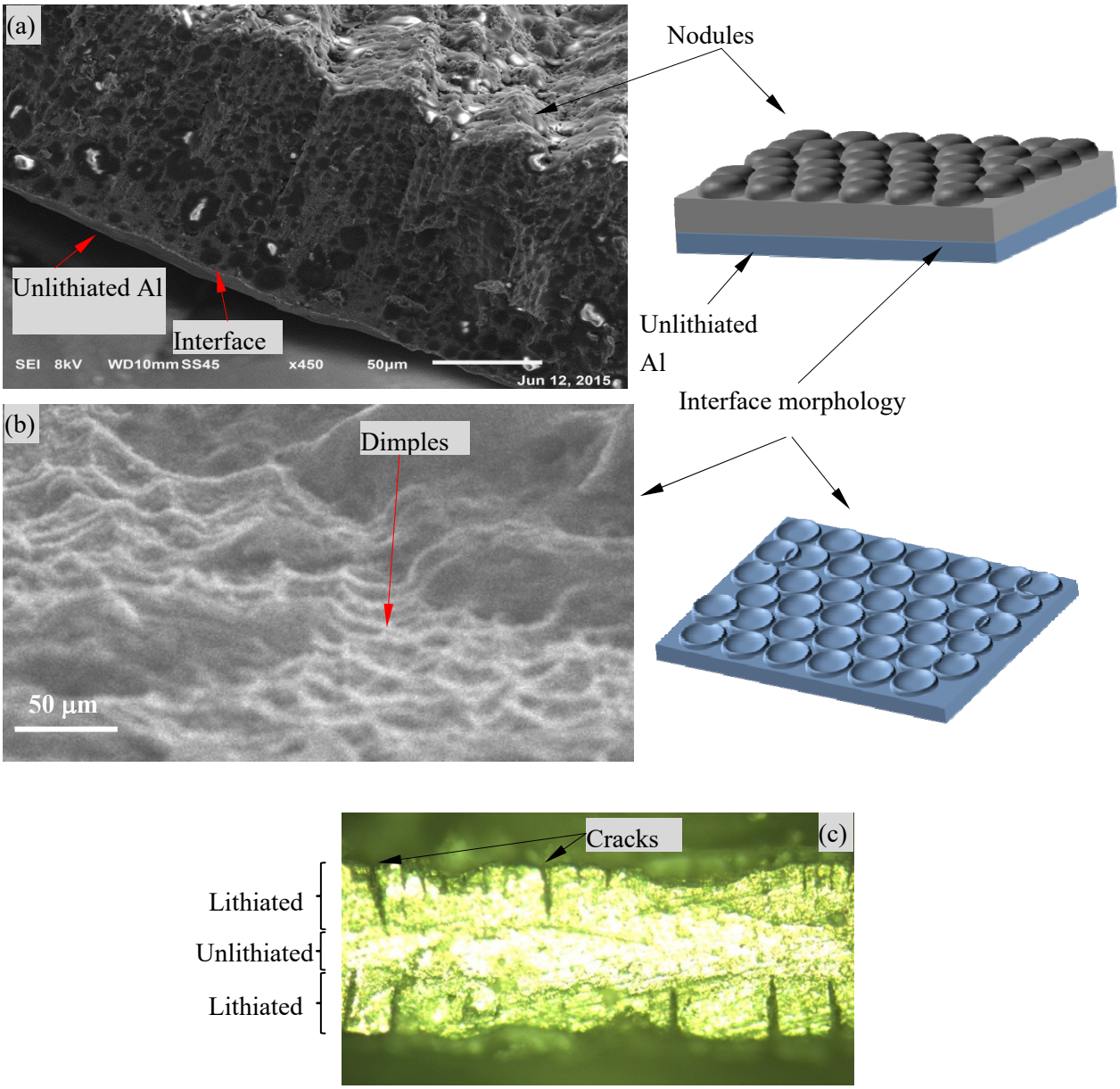

Figure 3. (a) SEM image showing the cross section of Al foil lithiated to 800 mAh/g. (b) SEM image showing the top view of the interface between lithiated and unlithiated portions, as marked in (a). (c) Optical micrograph showing crack formation in the lithiated portion of the cross section of a different lithiated specimen. Note that the cross section shown in (c) was polished using metallographic procedures.

- Now, we will attempt to explain the lithiation process and crack formation in the Al foils. A schematic of these processes is depicted in Figures 4a–4c. Lithiation occurs by the nucleation and growth of a new phase, LiAl, in the shape of nodules on the surface of Al foils (see Figures 4a and 2a). With continued lithiation, more nodules are nucleated and grow in size until they impinge onto the neighboring nodules and the entire surface is covered with the nodules (see Figure 4b). After this point, the lithiation progresses primarily in the thickness direction as the nodules are hindered to grow in the lateral direction. At a critical depth of lithiation, cracks form from the nodules and penetrate towards the interface between the lithiated and unlithiated portions (see Figure 4c).

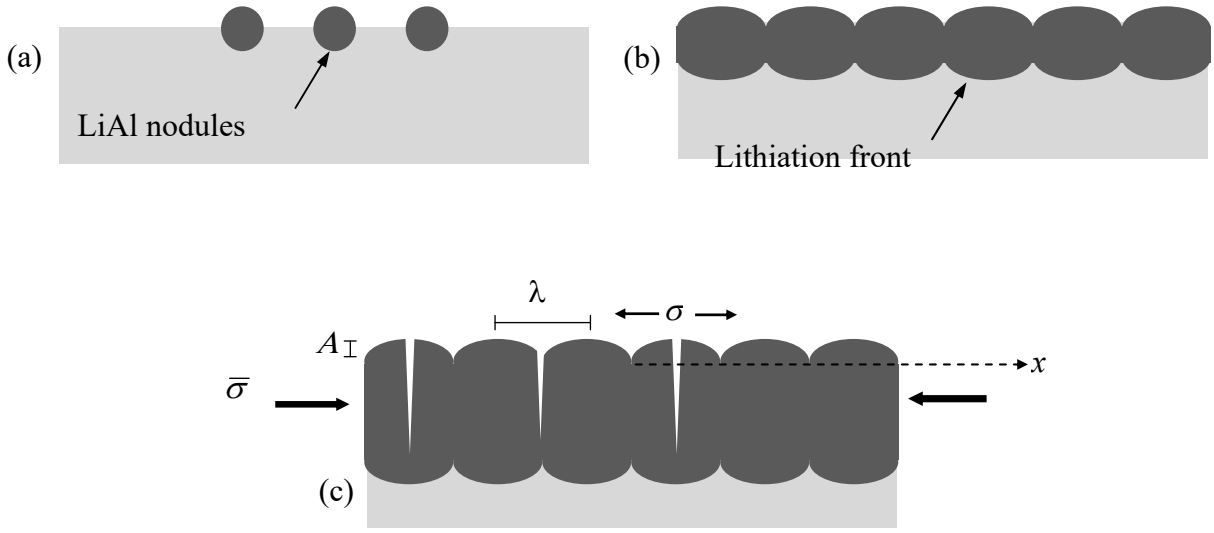

Figure 4. Schematics showing the various stages of lithiation of Al foils. (a) Nucleation and growth of nodules on the surface, (b) increase in the density of nodules on the surface and (c) columnar growth of nodules and crack formation.

- It is interesting to note crack formation in the lithiated portion during lithiation in spite of the fact that the overall lithiated portion is expected to be under a compressive stress as the lithiated portion is constrained against free expansion by the unlithiated portion. The formation of cracks can be attributed to local tensile stress concentrations on the surface as a result of the formation of nodules and their interactions with each other during lithiation. The effect of surface undulation and morphology change on the stress distribution of thin layers was studied in the past [37] and it was found that even a slightly wavy surface can easily result in stress concentration factors of up to 2–3. Assuming a sinusoidal surface morphology, it can be shown that the stress is obtained from the following equation [37]

$$\sigma = \bar{\sigma}\left(1 + \frac{4\pi A}{\lambda}\cos\left(\frac{2\pi x}{\lambda}\right)\right) \tag{2}$$

where $\overline{\sigma}$ is the bulk stress in the lithiated portion, and A and λ are the amplitude and wavelength of the surface undulation, respectively. The effect of nodule morphology is readily recognized from this equation. It is seen that the nodule height (A) and diameter (λ) affect the stress concentrations on the surface and at locations where stresses reach a critical tensile stress cracks are expected to occur. According to equation (2), tensile stress concentrations are expected to occur at nodule peaks for ($4\pi A/\lambda > 1$), which explains the observed cracks, as shown in Figures 2c and 2d. The formation of cracks at the nodule boundaries could be attributed to the impinging of nodules onto each other as well as the irregular shape of some nodule boundary junctions, amplifying local stress at these locations. It should be noted that other factors, such as the diffusion of Li ions through LiAl, kinetics and anisotropy of the interface reaction, microstructure, etc. could affect the stress distribution during lithiation.

- Next, we will explore the effect of current density, as an important parameter in lithiation, on the surface morphology of Al foils. Al foils were lithiated at various current densities of 2.5 mA/cm^2, 1.5 mA/cm^2, 0.75 mA/cm^2, and 0.07 mA/cm^2. The lithiation of the foils was continued up to a lithiation level of about 600 mAh/g except for the lithiation at the current density of 0.07 mA/cm^2, which was lithiated up to 182 mAh/g. This was due to a very low current density requiring a long time to reach the same lithiation level as in foils lithiated at other current densities. SEM images showing the surface morphology of the Al foils lithiated at various current densities are shown in Figures 5a–5d. Nodules are seen on the surface of all Al foils, suggesting a similar mechanism of phase transformation during lithiation of Al foils at varied current densities studied here. Example nodules are delimited with red dashed lines in the images for clarity. It is observed from the images that the nodules on the surface of the Al foil lithiated at the very low current density of 0.07 mA/cm^2 appear to be larger than those of Al foils lithiated at other current densities. The nodule size of Al foils was quantified and plotted in Figure 5e to elucidate the effect of current density on the surface morphology. An increase in the average nodule size of the lithiated Al anodes at the very low current density is evident from this plot. No significant differences in the average nodule size of Al foils lithiated at 2.5 mA/cm^2, 1.5 mA/cm^2, or 0.75 mA/cm^2 can be observed. It is noted that each nodule consisted of a colony of nanocrystallites of LiAl; the crystallite size of lithiated Al obtained from the XRD analysis will be presented later. Such a nodular morphology has also been observed in nanocrystalline electrodeposits [38,39]. Although crack formation in Al foils lithiated at varied current densities was not directly investigated here, the potential influence of current density on the crack formation and failure of LiAl through affecting the nodule size can be recognized. A detailed study of the crack formation in Al foils lithiated at varied current densities will be reported in future publications. It should be noted that the effect of current density on the failure of electrode materials was theoretically studied in the past [40,41]. In these studies, the effect of current density was shown to increase deformation gradients due to fast diffusion of Li ions in electrodes. The increase in deformation gradients results in an increase in stress and propensity to fracture in electrodes. Here, another potential mechanism by which current density could contribute to the fracture of electrodes is postulated.

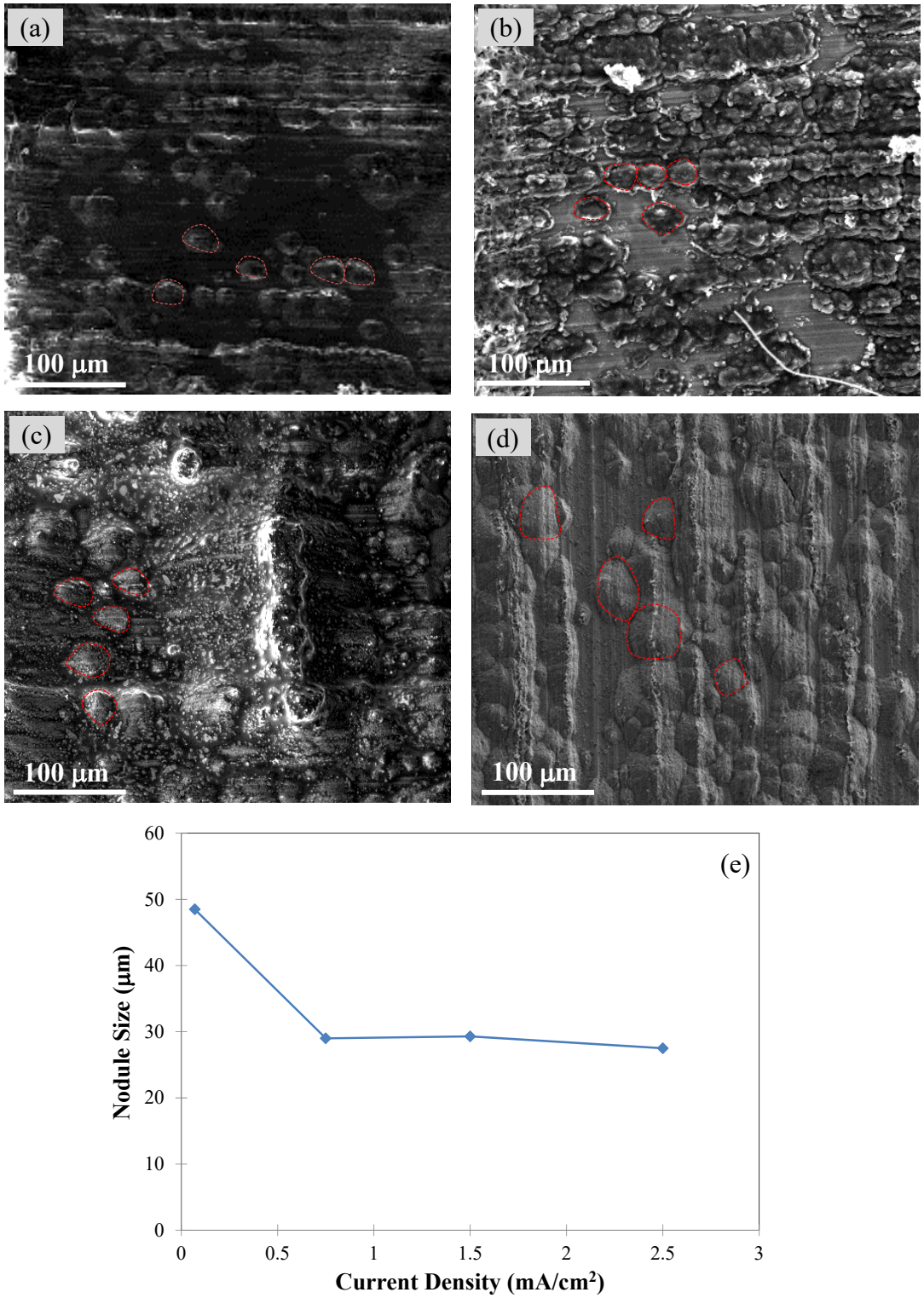

Figure 5. (a–d) SEM images showing the surface morphology of Al foils lithiated at 2.5 mA/cm^2, 1.5 mA/cm^2, 0.75 mA/cm^2, and 0.07 mA/cm^2, respectively. Example nodules are delimited with red dashed lines in the images. (e) Variation of surface nodule size of LiAl with current density.

3.2. XRD Analysis

XRD analysis was performed on Al foils lithiated at varied current densities in order to identify the lithiated phase, as well as to gain insight into the effect of current density on the crystallite size of the lithiated phase. The XRD spectrum of Al foil lithiated to 600 mAh/g at a current density of 1.5 A/cm^2 is shown in Figure 6a. The peaks at angles of 40° and 47° corresponding to LiAl are seen in the spectrum and confirm the formation of this phase during the lithiation of Al foil. The variation of crystallite size of LiAl with current density is depicted in Figure 6b. It is seen from Figure 6b that the crystallite size of LiAl is in the range of ~50–60 nm. This is in stark contrast with the crystallite size of unlithiated Al foils, which is expected to be in the microscale range.

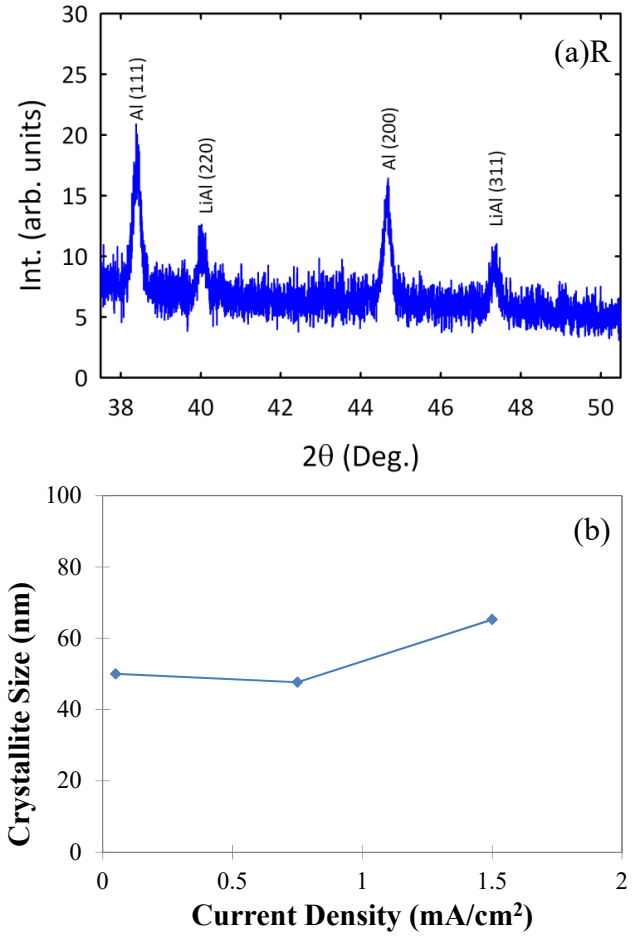

Figure 6. (a) XRD spectrum of a lithiated Al foil after lithiation to 600 mAh/g at a current density of 1.5 A/cm^2. (b) Variation of crystallite size with current density in electrochemical alloying of Al foil with Li.

3.3. Mechanical Test

Tensile specimens in the shape of a dogbone with a gage length of 5 mm and a width of 0.5 mm were fabricated from thin Al foils using photolithography and chemical etching. Al foils were

attached onto a four inch glass wafer previously cleaned with acetone. Another glass wafer was used to apply a pressure on the Al foils to reach a flat surface and to remove air pockets from under the Al foils. Then, the surface of the Al foil was spin coated with a photoresist. A thin stainless steel mask containing dogbone shaped openings was placed on the Al foils and subjected to a UV light. After UV exposure, the Al foils were immersed in a developer to achieve the desired patterns on the surface. Chemical etching was conducted by immersing the Al foils in an Al etchant for about one hour. The lift-off of thin foil dogbone specimens was carried out by rinsing the wafer in acetone. The dogbone specimens were gently collected from acetone and placed in a sealed container until testing. A schematic of the dogbone specimen is shown in Figure 7a.

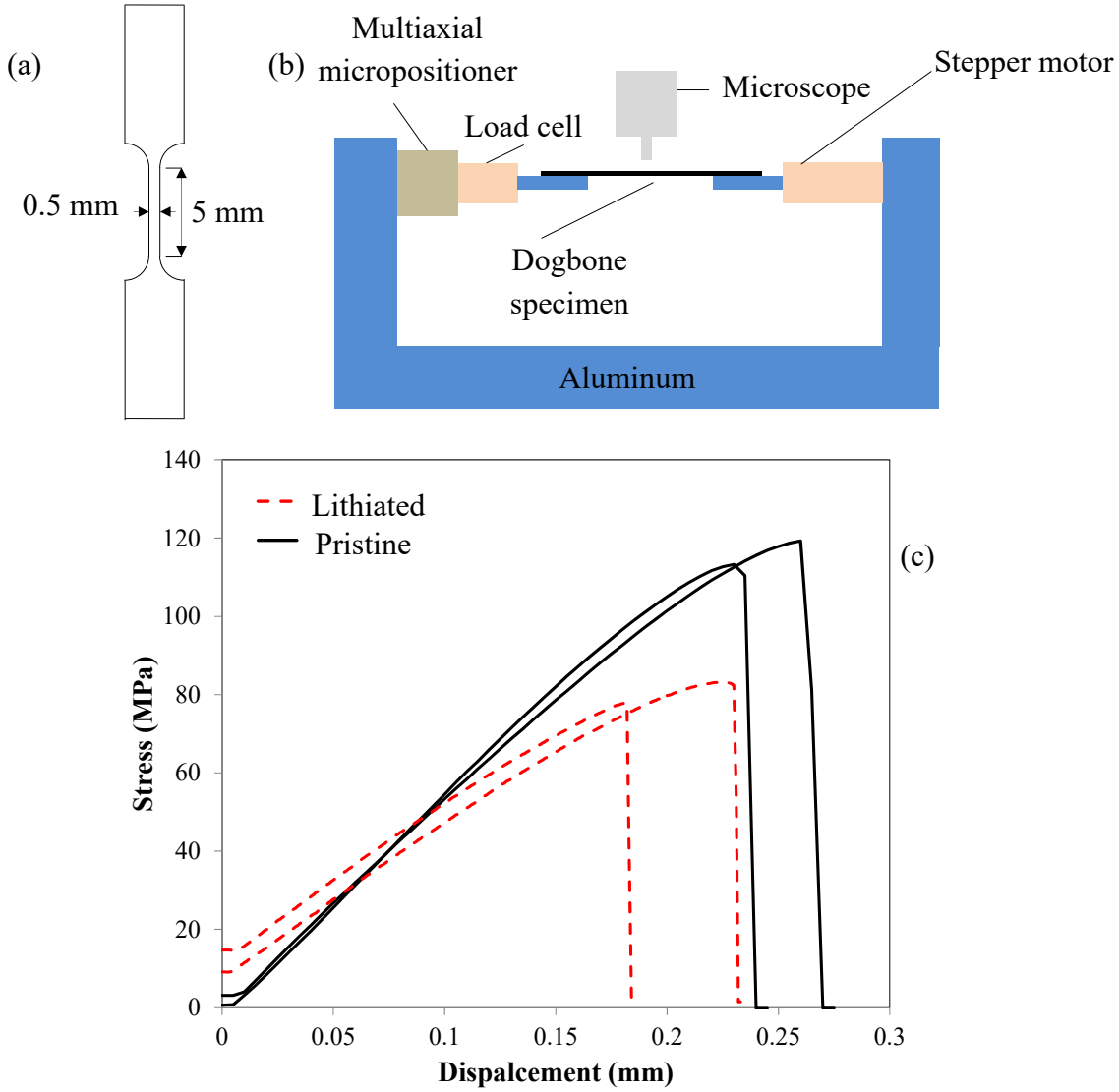

Figure 7. Schematics of (a) the dogbone specimens and (b) the microtensile stage used for mechanical testing. (c) Nominal stress vs displacement curves of pristine and lithiated dogbone specimens.

The Al dogbone tensile specimens were used as the anode electrode and mounted in the electrochemical half-cell, as described previously. Specimens were lithiated in the glovebox to a charge level of 365 mAh/g at a current density of 0.17 mA/cm^2. Since fully lithiated Al foils become pulverized and disintegrated, it is not possible to perform the tensile test using this setup. Thus, partially lithiated Al foils were used in the tensile test to examine the effect of lithiation on the mechanical behavior of Al foils. After lithiation, the fixture on which the dogbone specimens were mounted was placed in a polypropylene tube, thoroughly sealed, and transferred to a microtensile stage for mechanical testing (see Figure 7b). The lithiated specimens were clamped at both ends in the microstensile stage which was comprised of a miniature load cell with a resolution of 2×10^{-5} N to obtain load measurements and a stepper motor micropositioner with a resolution of 50 nm to induce deformation in the specimen. A manual xyz micropositioner was used for the alignment of the tensile specimens. Mechanical testing was performed at a displacement rate of 1 μm/s. The images of the specimen surface during loading were captured with an optical microscope. It is noted that the lithiated specimens were exposed to air for less than a few minutes during the tensile tests.

The nominal stress vs displacement curves of unlithiated (pristine) and lithiated Al dogbone specimens are shown in Figure 7c. The nominal stress was calculated using the load and the cross sectional area, accounting for the increase in the cross sectional area due to volumetric expansion during lithiation. It is seen that both stiffness and tensile strength decreased in the lithiated specimens compared to those in the unlithiated specimens.

The top view of the unlithiated and lithiated dogbone specimens after failure is shown in Figures 8a and 8b, respectively. A transition in the failure mechanism from ductile shear to brittle is demonstrated from the change in the orientation of the fracture surface with respect to the loading direction, as marked in these figures.

An SEM cross sectional view of the fracture surface of the lithiated specimen is depicted in Figure 8c. A close examination of the cross section of the specimen revealed that the fracture surface consisted of unlithiated Al in the middle sandwiched by layers of LiAl on both sides. The unlithiated portion of the fracture surface appeared to be flat in the middle flanked by two slanted planes. The flat segment of the unlithiated Al exhibited dimples indicative of fracture due to void nucleation, growth, and coalescence, which is a primary ductile fracture mechanism [42,43]. The two slanted planes are understood to be the result of ductile shear fracture in the unlithiated portion of the fracture surface. A schematic showing the morphological characteristics of the fracture surface differentiating fracture mechanisms is depicted in Figure 8c. It is seen from the figure that the lithiated portion of the fracture surface seemed to be flat at the length scale equal to the thickness of the specimen. This indicates that fracture in the lithiated portion is of brittle nature and supports the observation made from the change in the direction of fracture plane, as seen in Figures 8a and 8b. It follows from the discussion above that ductile Al becomes brittle and exhibits a lower resistance to fracture as a result of lithiation. This observation of the change in the mechanical behavior of Al anodes is in contrast with the studies focused on Si anodes, where lithiation was shown to induce plastic behavior in lithiated Si anodes [44–47]. In view of the difference in the effect of lithiation on the mechanical behavior of Si and Al anodes, which leads to different fracture characteristics in these two anodes, it becomes evident that studying the mechanical properties of anodes is of significant

importance in obtaining a fundamental understanding of the failure mechanisms of anodes in Li-ion batteries.

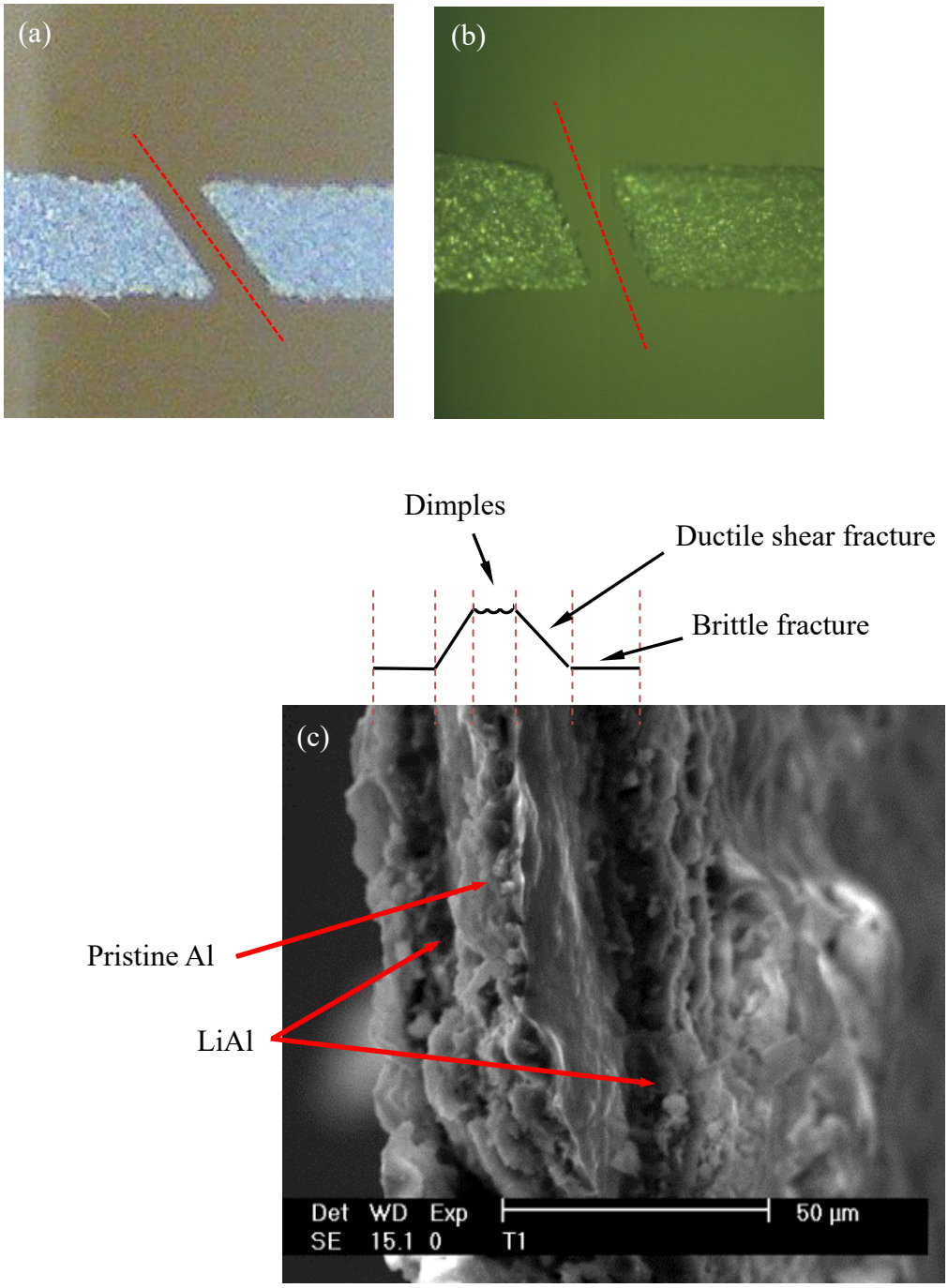

Figure 8. Images showing the fracture plane in (a) pristine and (b) lithiated dogbone specimens. A transition in the fracture mode from ductile shear to brittle can be inferred from the change in the orientation of the fracture plane. (c) SEM image of the fracture surface of the lithiated specimen revealing the fracture mechanisms in the pristine and lithiated portions of the cross section.

4. Conclusions

In this study, the evolution of surface morphology and crack formation during the lithiation of Al anodes were investigated. The effect of current density on lithiation and the change in the mechanical behavior of lithiated Al anodes were elucidated. The following conclusions were drawn:

- Lithiation in Al foils was initiated by the formation and growth of LiAl nodules on the surface and continued by columnar growth in the thickness direction.
- Cracks were observed to occur near the peak of nodules and also at the boundaries between the nodules. The development of local tensile stress concentration sites due to nodule formation while the overall lithiated portion is under compressive stress is suggested as the mechanism of the crack formation during lithiation.
- The XRD analysis indicated a phase transformation of the microcrystalline Al to nanocrystalline LiAl with an average crystallite size of about 50–60 nm.
- Mechanical tensile tests showed a reduction in the stiffness and fracture strength of LiAl. A transition from ductile shear to brittle fracture in lithiated Al foils was demonstrated using SEM and optical microscopy.

Acknowledgements

The authors are grateful to Dr. Burjor Captain for allowing access to a glovebox for some of the experiments in this study. Dr. Joshua Cohn is thanked for performing the XRD measurements.

Conflict of Interest

All authors declare that there is no conflict of interest in this paper.

References

1. Hatchard TD, Dahn JR (2004) In Situ XRD and Electrochemical Study of the Reaction of Lithium with Amorphous Silicon. *J Electrochem Soc* 151: A838–A842.
2. Larcher D, Beattie S, Morcrette M, et al. (2007) Recent findings and prospects in the field of pure metals as negative electrodes for Li-ion batteries. *J Mater Chem* 17: 3759–3772.
3. Nitta N, Yushin G (2013) High-Capacity Anode Materials for Lithium-Ion Batteries: Choice of Elements and Structures for Active Particles. *Part Part Syst Charact* 31: 317–336.
4. Beaulieu LY, Cumyn VK, Eberman KW, et al. (2001) A system for performing simultaneous in situ atomic force microscopy/optical microscopy measurements on electrode materials for lithium-ion batteries. *Rev Sci Instrum* 72: 3313–3319.
5. McDowell MT, Lee SW, Nix WD, et al. (2013) 25th Anniversary Article: Understanding the Lithiation of Silicon and Other Alloying Anodes for Lithium-Ion Batteries. *Adv Mater* 25: 4966–4985.
6. Beaulieu LY, Eberman KW, Turner RL, et al. (2001) Colossal Reversible Volume Changes in Lithium Alloys. *Electrochem Solid-State Lett* 4: A137–A140.

7. Winter BM, Besenhard JO, Spahr ME, et al. (1998) Insertion Electrode Materials for Rechargeable Lithium Batteries. *Adv Mater* 10: 725–763.
8. Kasavajjula U, Wang C, Appleby AJ (2007) Nano- and bulk-silicon-based insertion anodes for lithium-ion secondary cells. *J Power Sources* 163: 1003–1039.
9. Liu XH, Zheng H, Zhong L, et al. (2011) Anisotropic swelling and fracture of silicon nanowires during lithiation. *Nano Lett* 11: 3312–3318.
10. Nishikawa K, Munakata H, Kanamura K (2013) In-situ observation of one silicon particle during the first charging. *J Power Sources* 243: 630–634.
11. Kalnaus S, Rhodes K, Daniel C (2011) A study of lithium ion intercalation induced fracture of silicon particles used as anode material in Li-ion battery. *J Power Sources* 196: 8116–8124.
12. Rhodes K, Dudney N, Lara-Curzio E, et al. (2010) Understanding the Degradation of Silicon Electrodes for Lithium-Ion Batteries Using Acoustic Emission. *J Electrochem Soc* 157: A1354–A1360.
13. Zhao K, Pharr M, Cai S, et al. (2011) Large Plastic Deformation in High-Capacity Lithium-Ion Batteries Caused by Charge and Discharge. *J Am Ceram Soc* 94: s226–s235.
14. Sethuraman VA, Nguyen A, Chon MJ, et al. (2013) Stress Evolution in Composite Silicon Electrodes during Lithiation/Delithiation. *J Electrochem Soc* 160: A739–A746.
15. Bower AF, Guduru PR, Sethuraman VA (2011) A finite strain model of stress, diffusion, plastic flow, and electrochemical reactions in a lithium-ion half-cell. *J Mech Phys Solids* 59: 804–828.
16. Melendres CA, Sy CC (1978) Structure and Cyclic Discharge Behavior of LiAl Electrodes. *J Electrochem Soc* 125: 727–731.
17. Wen CJ, Boukamp BA, Huggins RA (1979) Thermodynamic and Mass Transport Properties of "LiAl". *J Electrochem Soc* 126: 2258–2266.
18. Besenhard JO, Hess M, Komenda P (1990) Dimensionally Stable Li-Alloy Electrodes for Secondary Batteries. *Solid State Ionics* 41: 525–529.
19. Garreau M, Thevenin J, Fekir M, et al. (1983) On the processes responsible for the degradation of the aluminum-lithium electrode used as anode materials in lithium aprotic electrolyte batteries. *J Power Sources* 9: 235–238.
20. Zaghib K, Gauthier M, Armand M (2003) Expanded metal a novel anode for Li-ion polymer batteries. *J Power Sources* 119–121: 76–83.
21. Lei X, Wang C, Yi Z, Liang Y, et al. (2007) Effects of particle size on the electrochemical properties of aluminum powders as anode materials for lithium ion batteries. *J Alloys Compd* 429: 311–315.
22. Hamon Y, Brousse T, Jousse F, et al. (2001) Aluminum negative electrode in lithium ion batteries. *J Power Sources* 97–98: 185–187.
23. Au M, McWhorter S, Ajo H, et al. (2010) Free standing aluminum nanostructures as anodes for Li-ion rechargeable batteries. *J Power Sources* 195: 3333–3337.
24. Kuksenko SP (2013) Aluminum foil as anode material of lithium-ion batteries: Effect of electrolyte compositions on cycling parameters. *Russ J Electrochem* 49: 67–75.
25. Sharma SK, Kim MS, Kim DY, et al. (2013) Al nanorod thin films as anode electrode for Li ion rechargeable batteries. *Electrochim Acta* 87: 872–879.

26. El Abedin SZ, Garsuch A, Endres F (2012) Aluminium Nanowire Electrodes for Lithium-Ion Batteries. *Aust J Chem* 65: 1529–1533.
27. Leite MS, Ruzmetov D, Li Z, et al. (2014) Insights into capacity loss mechanisms of all-solid-state Li-ion batteries with Al anodes. *J Mater Chem A* 2: 20552–20559.
28. Beaulieu LY, Hatchard TD, Bonakdarpour A, et al. (2003) Reaction of Li with Alloy Thin Films Studied by In Situ AFM. *J Electrochem Soc* 150: A1457–A1464.
29. Owen JR, Maskell WC, Steele BCH, et al. (1984) Thin film lithium aluminium negative plate material. *Solid State Ionics* 13: 329–334.
30. Liu Y, Hudak NS, Huber DL, et al. (2011) In situ transmission electron microscopy observation of pulverization of aluminum nanowires and evolution of the thin surface Al_2O_3 layers during lithiation-delithiation cycles. *Nano Lett* 11: 4188–4194.
31. Hudak NS, Huber DL (2012) Size Effects in the Electrochemical Alloying and Cycling of Electrodeposited Aluminum with Lithium. *J Electrochem Soc* 159: A688–A695.
32. John C, Huggins RA (1980) Electrochemical Investigation of Solubility and Chemical Diffusion of Lithium in Aluminum. *Metall Mater Trans B* 11: 131–137.
33. Pollak E, Lucas IT, Kostecki R (2010) A study of lithium transport in aluminum membranes. *Electrochem Commun* 12: 198–201.
34. McDowell MT, Lee SW, Ryu I, et al. (2011) Novel size and surface oxide effects in silicon nanowires as lithium battery anodes. *Nano Lett* 11: 4018–4025.
35. Mittemeijer EJ, Welzel U (2008) The "state of the art" of the diffraction analysis of crystallite size and lattice strain. *Zeitschrift Fur Krist* 223: 552–560.
36. Transactions ECS, Society TE (2011) Nanostructured lithium-aluminum alloy electrodes for lithium-ion batteries. *ECS Trans* 33: 1–13.
37. Gao H (1990) Stress concentration at slightly undulating. *J Mech Phys Solids* 39: 443–458.
38. Ruan S, Schuh CA (2008) Mesoscale structure and segregation in electrodeposited nanocrystalline alloys. *Scr Mater* 59: 1218–1221.
39. Bastos A, Zaefferer S, Raabe D, et al. (2006) Characterization of the microstructure and texture of nanostructured electrodeposited NiCo using electron backscatter diffraction (EBSD). *Acta Mater* 54: 2451–2462.
40. Zhao K, Pharr M, Vlassak JJ, et al. (2010) Fracture of electrodes in lithium-ion batteries caused by fast charging. *J Appl Phys* 108: 073517.
41. Grantab R, Shenoy VB (2012) Pressure-Gradient Dependent Diffusion and Crack Propagation in Lithiated Silicon Nanowires. *J Electrochem Soc* 159: A584–A591.
42. Rice BJR (1969) On the ductile enlargement of voids in triaxial stress fields. *J Phys Mech Solids* 17: 201–217.
43. Ghahremaninezhad A, Ravi-Chandar K (2012) Ductile failure behavior of polycrystalline Al 6061-T6. *Int J Fract* 174: 177–202.
44. Kushima A, Huang JY, Li J (2012) Quantitative Fracture Strength and Plasticity Measurements of Lithiated Silicon Nanowires by In Situ TEM Tensile Experiments. *ACS Nano* 6: 9425–9432.
45. Zhao K, Pharr M, Wan Q, et al. (2012) Concurrent Reaction and Plasticity during Initial Lithiation of Crystalline Silicon in Lithium-Ion Batteries. *J Electrochem Soc* 159: A238–A243.

46. Zhao K, Wang WL, Gregoire J, et al. (2011) Lithium-assisted plastic deformation of silicon electrodes in lithium-ion batteries: a first-principles theoretical study. *Nano Lett* 11: 2962–2967.
47. Nadimpalli SPV, Sethuraman VA, Bucci G, et al. (2013) On Plastic Deformation and Fracture in Si Films during Electrochemical Lithiation/Delithiation Cycling. *J Electrochem Soc* 160: A1885–A1893.

AIMS Press